

Surface Atomic Structure and Functionality of Metallic Nanoparticles: A Case Study of Au–Pd Nanoalloy Catalysts

Valeri Petkov,^{*,†} Binay Prasai,[†] Sarvjit Shastri,[‡] Jong-Woo Kim,[‡] Shiyao Shan,[§] Haval R. Kareem,[§] Jin Luo,[§] and Chuan-Jian Zhong[§]

[†]Department of Physics, Central Michigan University, Mt. Pleasant, Michigan 48859, United States

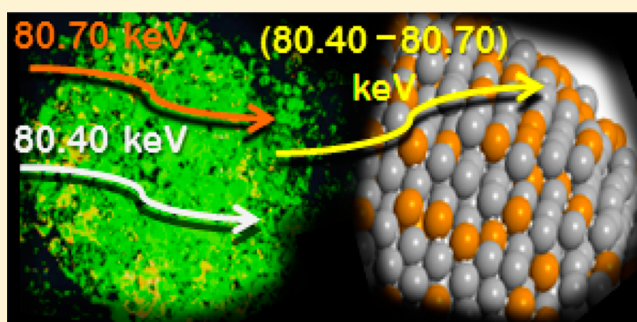
[‡]X-ray Science Division, Advanced Photon Source, Argonne National Laboratory, Argonne, Illinois 60439, United States

[§]Department of Chemistry, State University of New York at Binghamton, Binghamton, New York 13902, United States

S Supporting Information

ABSTRACT: The surface atomic structure of metallic nanoparticles (NPs) plays a key role in shaping their physicochemical properties and response to external stimuli. Not surprisingly, current research increasingly focuses on exploiting its prime characteristics, including the amount, location, coordination, and electronic configuration of distinct surface atomic species, as tunable parameters for improving the functionality of metallic NPs in practical applications. The effort requires clear understanding of the extent to which changes in each of these characteristics would contribute to achieving the targeted functionality. This, in the first place, requires good knowledge of the actual surface of metallic NPs

at atomic level. Through a case study on Au–Pd nanoalloy catalysts of industrial and environmental importance, we demonstrate that the surface atomic structure of metallic NPs can be determined in good detail by resonant high-energy X-ray diffraction (HE-XRD). Furthermore, using our experimental surface structure and CO oxidation activity data, we shed new light on the elusive origin of the remarkable catalytic synergy between surface Au and Pd atoms in the nanoalloys. In particular, we show that it arises from the formation of a specific “skin” on top of the nanoalloys that involves as many unlike, i.e., Au–Pd and Pd–Au, atomic pairs as possible given the overall chemical composition of the NPs. Moreover, unlike atoms from the “skin” interact strongly, including both changing their size and electronic structure in inverse proportions. That is, Au atoms shrink and acquire a partial positive charge of 5d-character whereas Pd atoms expand and become somewhat 4d-electron deficient. Accordingly, the reactivity of Au increases whereas Pd atoms become less reactive, as compared to atoms at the surface of pure Au and Pd NPs, respectively. Ultimately, this renders Au–Pd alloy NPs superb catalysts for CO oxidation reaction over a broad range of alloy compositions. Our findings are corroborated by DFT calculations based on a refined version of d-band center theory on the catalytic properties of late transition metals and alloys. We discuss opportunities for improving the accuracy of current theory on surface-controlled properties of metallic NPs through augmenting the theory with surface structure data obtained by resonant XRD.



1. INTRODUCTION

Largely, the physicochemical properties of a bulk (μm -sized) metallic material are determined by the type and arrangement of atoms inside it and so do not depend on the size, shape, and surface of the material.^{1,2} However, as the size of a metallic material decreases toward nanoscale dimensions, the physicochemical properties of the material increasingly become dependent on the type and arrangement of atoms at its surface. Thus, a metallic material confined to nanosized dimensions can exhibit a novel functionality that is induced and controlled mainly, if not entirely, by its surface. An example of a novel functionality emerging as a bulk metal is reduced to nanoscale dimensions is the catalytic activity of Au NPs. While bulk Au is very inert chemically, i.e., unreactive, Au NPs (<10 nm) catalyze a number of reactions, including low-temperature oxidation of CO, water gas-shift reaction, alcohol oxidation to

acids and aldehydes, and others.^{3–5} For comparison, bulk Pd is less inert than Au and so surfaces of Pd have long been employed as catalysts in several useful applications, such as reducing the amounts of pollutants in automotive emission, removing contaminants from syngas, and others. Perhaps not surprisingly, the catalytic activity of Pd has been found to increase significantly at the nanoscale.^{6–10}

It is well-known that catalytic reactions over metal surfaces proceed through creating and breaking of bonds between valence electrons at the Fermi level of surface metal atoms and frontier orbitals of reactants, including reaction intermediates and products. Hence, largely, the number and character of

Received: January 5, 2017

Revised: February 9, 2017

Published: March 23, 2017

valence electrons at the Fermi level, or the valence electron density of states (DOS) near the Fermi energy, on surface atomic sites is what determines the catalytic properties of metals and alloys. For late transition metals (TMs) such as Au and Pd, the valence electrons available for bonding are of md , $(m + 1)s$, and $(m + 1)p$ character, where m is the number of the respective row in the periodic table. In particular, Au and Pd may be considered to have 11 and 10 valence electrons since their electron configuration is $5d^{10}6s^1$ and $4d^{10}5s^0$, respectively. However, at the bulk scale, a small number of the valence d electrons of Pd and Au are pushed into higher-energy s and p states through a process known as $sp-d$ hybridization. Hence, the actual valence electron structure of bulk Pd and Au is $4d^{9.45}(sp)^{0.6}$ and $5d^{9.66}(sp)^{1.4}$, respectively.¹¹ Typically, the interaction between the adsorbate orbitals and nearly free valence electrons of s - and p -character is bonding and, furthermore, does not vary much between different late TMs. A significant variation in binding though may come from the interaction between the adsorbate orbitals and valence electrons of d -character. In particular, studies have found that the catalytic activity and selectivity of surfaces of late TMs and their alloys are influenced by the particular degree of $sp-d$ hybridization, width and position of surface d -electron bands with respect to the Fermi energy, overlap between the adsorbate orbitals and occupied surface d -electron DOS, and others.^{12–15} Within the framework of adsorbate orbital–valence d -electrons interactions, the negligible reactivity of bulk Au can be explained by the fact that its $5d$ -band is fully occupied and positioned well below the Fermi energy, which makes the valence electrons of $5d$ -character necessary for the formation of chemisorption bonds largely inaccessible. The apparent reactivity of Pd surfaces can then be explained by the fact that the $4d$ -band of Pd extends through the Fermi level, that is, $4d$ -electron DOS at the Fermi energy is high enabling the formation of sufficiently strong chemisorption bonds.¹⁶ Several explanations for the suddenly appeared and further increased catalytic activity of Au and Pd NPs, respectively, have been put forward, including the presence of a large number of low-coordinated surface atoms, surface stresses intrinsic to metallic NPs and related to them changes in the width and energy position of surface d -bands, quantum confinement, NP support effects, and others.^{3,12–16} Note, here we use the term “reactivity” to describe the generic interaction of TM surfaces with adsorbates. A good catalyst though should interact with adsorbates with ample strength so that they can react on its surface but weakly enough to release the reaction intermediates and product when the reaction ends. Besides, for the catalytic reaction to proceed with a high rate, both the strength of adsorbate–metal surface interaction and also the energy barriers between reactants and products, that is the energy needed to break or weaken a bond between adsorbates and surface metal atoms, are important. Therefore, catalyst design has long aimed at optimizing the often correlated adsorption energy and reaction barriers through engineering the reactivity of catalytically active sites on TM surfaces.^{12–15}

Along this line of research, Au–Pd alloy NPs have emerged as excellent catalysts for a number of reactions of industrial importance.^{12–16} Despite the consistent research effort, the origin of the largely improved catalytic activity and stability of Au–Pd alloy NPs as compared to the end members of the alloy, that is pure Au and Pd NPs, is still under debate. In particular, it has been suggested that the improvement is due to cooperation between nearby surface Au and Pd atoms in the

NPs, also known as a “bifunctional” mechanism, involving mere exchange (“spillover”) of adsorbed oxygen species. The so-called “atomic ensemble effect” has also been evoked and the improvement explained in terms of specific configurations of surface Au and Pd atoms such as, for example, short chains of Pd atoms surrounded by Au atoms. In addition, it has been argued that the improvement arises from charge exchange between surface Au and Pd atoms, known as a “ligand effect”, such that the former gain $6(sp)$ electrons and lose $5d$ electrons whereas the latter lose $5(sp)$ electrons and gain $4d$ electrons.^{12,17–22} Here we focus on revealing that origin by (i) determining the surface atomic structure of three members of the family of Au–Pd alloy NPs, (ii) evaluating their catalytic activity for low-temperature CO oxidation, and (iii) comparing the experimental surface structure and catalytic data side by side. Note, the CO oxidation reaction is prototypical for heterogeneous catalysis and so widely used as a litmus test for probing the catalytic activity and stability of NPs based on TMs and their alloys. Besides, it is important to the areas of pollution control and development of devices for clean energy conversion such as fuel cells.^{3,21,22} To avoid possible NP size effects, we produce and study Au–Pd alloy NPs with the same size and low dispersity. Also, to avoid possible NP support effects, we deposit the NPs on fine carbon powder, which is considered an inactive component of the CO oxidation reaction.²³ More details regarding the mechanism of CO oxidation reaction over TM-based NPs can be found in the Methods section of the Supporting Information.

2. EXPERIMENTAL SECTION

Binary Au–Pd alloy NPs were synthesized by a wet chemical route described in the Methods section of the Supporting Information. Pure Au NPs were also synthesized and used as a reference point in the surface atomic structure determination and analysis. As-synthesized pure Au and Au–Pd alloy NPs were deposited on fine carbon powder and activated for catalytic applications by a controlled thermochemical treatment including heating at elevated temperature first in oxygen and then in hydrogen atmosphere. More details of the post-synthesis treatment protocol can be found in the Methods section of the Supporting Information.

The overall chemical composition of Au–Pd alloy NPs was determined by inductively coupled plasma atomic emission spectroscopy (ICP-AES) and cross-checked by energy dispersive X-ray spectroscopy (EDS) experiments, both described in the Methods section of the Supporting Information. Experimental data showed that, as desired, one of the three members of the family of Au–Pd alloy NPs has a chemical composition of Au_9Pd_{91} , i.e., is a Pd-rich nanoalloy; another of the members has a chemical composition of $Au_{69}Pd_{31}$, i.e., is a Pd-poor nanoalloy; and the third member has a chemical composition of $Au_{45}Pd_{55}$, i.e., is an Au–Pd nanoalloy wherein the relative ratio of Au to Pd species is close to 50:50. Note, following the widely adopted definition, here we use the term “alloy” to describe any mixture of distinct metallic species, irrespective of the degree of their mixing and way of mixing.²⁴

The size, shape, and chemical pattern of Au_xPd_{100-x} alloy NPs ($x = 9, 45, 69$, and 100) were determined by transmission electron microscopy (TEM), high-angle annular dark field scanning transmission electron microscopy (HAADF-STEM), and EDS, as described in the Methods section of the Supporting Information. Exemplary TEM and high-resolution (HR) TEM images are shown in Figure S1. Exemplary

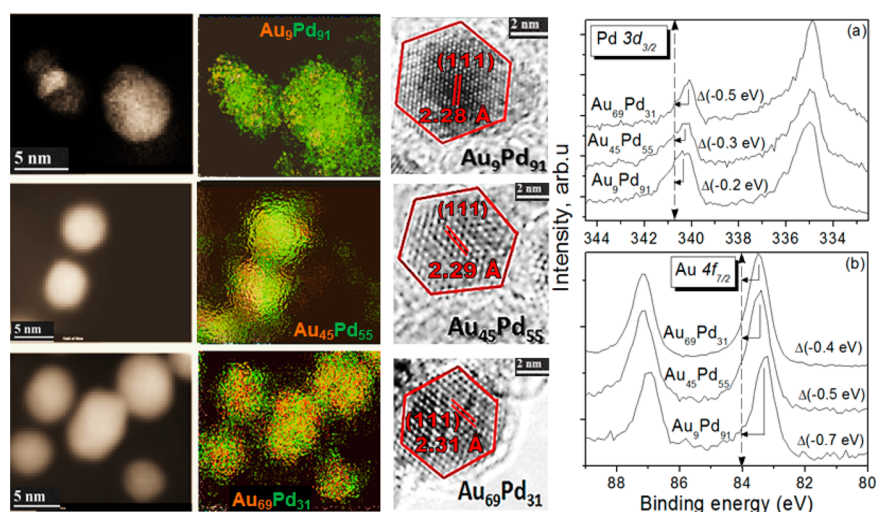


Figure 1. (left) Representative HAADF-STEM images and corresponding EDS elemental maps of Au₉Pd₉₁, Au₄₅Pd₅₅, and Au₆₉Pd₃₁ NPs. Au atoms are in yellow, and Pd atoms are in green. Maps indicate that the surface of Au₉Pd₉₁ NPs is likely to be enriched in Au species whereas Au₄₅Pd₅₅ and Au₆₉Pd₃₁ NPs are nearly uniform alloys. (middle) Representative HR-TEM images of Au₉Pd₉₁, Au₄₅Pd₅₅, and Au₆₉Pd₃₁ NPs. Solid red lines outlining the NPs emphasize their polyhedral shape. Lattice fringes (red bars) reveal the good degree of crystallinity in the NPs. (right) Typical XPS (a) Pd 3d_{3/2} and (b) Au 4f_{7/2} spectra for Au₉Pd₉₁, Au₄₅Pd₅₅, and Au₆₉Pd₃₁ NPs. The shift, Δ , in the core-level binding energy of Pd and Au atoms in the respective NPs is evaluated (arrows) with respect to the Pd 3d_{3/2} (340.7 eV) and Au 4f_{7/2} (84.0 eV) lines (vertical broken lines) characteristic to bulk Pd and Au metals, respectively.

HAADF-STEM images and EDS maps are shown in Figure 1 (left). TEM images reveal that both pure Au and Au–Pd alloy NPs are with an average size of approximately 6.5 (± 0.5) nm and fairly low dispersity. A closer inspection of the HR-TEM images in Figure S1 (last row) and Figure 1 (middle panel) shows that the NPs possess a high degree of crystallinity and are polyhedral in shape. Hence, from a structural point of view, they can be considered as almost complete nanocrystallites. Elemental maps in Figure 1 (middle panel) hint that Au₆₉Pd₃₁ and Au₄₅Pd₅₅ NPs are nearly homogeneous nanoalloys whereas Au₉Pd₉₁ NPs are likely to exhibit an Au-enriched surface.

The near-surface chemical composition and electronic structure of Au_xPd_{100-x} alloy NPs ($x = 9, 45,$ and 69) were studied by X-ray photoelectron spectroscopy (XPS). Details of the XPS experiments and the utility of XPS data obtained are discussed in the Methods section of the Supporting Information. Typical XPS Au 4f and Pd 3d spectra and shifts in the core-level binding energy of near-surface Au and Pd atoms in Au_xPd_{100-x} alloy NPs ($x = 9, 45,$ and 69) are shown in Figure 1 (right). The shifts are negative for both Au and Pd atoms and, furthermore, similar in magnitude (< 1 eV) to those found with bulk Au–Pd alloys and annealed thin Au–Pd films.^{25,26} The observation indicates that near-surface Au and Pd atoms in Au_xPd_{100-x} alloy NPs ($x = 9, 45,$ and 69) are well intermixed together. For reference, as found by experiment, pure Au and Pd NPs (< 10 nm) exhibit a positive 4f and 3d core level shift relative to bulk Au and Pd, respectively.^{27,28} Evidently, the electronic structure of near-surface Au and Pd atoms in Au_xPd_{100-x} alloy NPs ($x = 9, 45,$ and 69) is significantly different from that of near-surface Au and Pd atoms in pure Au and Pd NPs, respectively. Besides, as the asymmetry of Pd 3d_{3/2} and the Au 4f_{7/2} lines indicates, near-surface Au and Pd atoms in the alloy NPs are rather diverse in terms of electronic structure, likely due to variations in their coordination environment.^{29,30} Notably, the XPS spectra do not exhibit signatures of oxygen species (i.e., no peak at 343 eV; compare the XPS spectra in Figure 1 (right) with those in

Figure 5 in ref 31), indicating that, under ambient conditions, surface Au and Pd atoms in Au_xPd_{100-x} alloy NPs ($x = 9, 45,$ and 69) persist as Au⁰ and Pd⁰ metallic species. XPS spectra in the Pd 3p_{3/2}/O 1s region (510–550 eV) summarized in Figure S12 indicate the same. The near surface composition of Au_xPd_{100-x} alloy NPs ($x = 9, 45,$ and 69) was determined by analyzing the areas of the respective XPS peaks and found to be “Au₂₀Pd₈₀”, “Au₄₉Pd₅₁”, and “Au₆₂Pd₃₈”, respectively. The result corroborates the findings of EDS experiments, namely, that the surface and overall chemical composition of Au–Pd alloy NPs studied here are not quite the same. Besides, it is in line with the findings of studies on thin Au–Pd films annealed at 400 °C,²⁷ which is the temperature of postsynthesis treatment of Au_xPd_{100-x} alloy NPs ($x = 9, 45,$ and 69) (see the Methods section of the Supporting Information). Independent resonant HE-XRD and element-specific atomic pair distribution function (PDF) studies described below arrived at the same conclusion.

The catalytic activity of Au_xPd_{100-x} alloy NPs ($x = 9, 45,$ and 69) for CO oxidation reaction was determined on a custom-built system described in the Methods section of the Supporting Information. A representative set of CO conversion curves is shown in Figure S3. Analysis of the catalytic data showed that the temperature at which 50% of CO conversion is achieved, known as $T_{1/2}$ (or T_{50}), for Au₉Pd₉₁, Au₄₅Pd₅₅, and Au₆₉Pd₃₁ alloy NPs is 161, 159, and 211 °C, respectively. For comparison, $T_{1/2}$ for carbon supported pure Pd and Au NPs, as obtained on the same equipment, is 146 and 283 °C, respectively. Experimental data for the so-called turnover frequency, TOF, indicated the same trend (see Figure 8a introduced later on). Notably, in line with the findings of other studies,^{12,32–34} our catalytic data showed that the CO oxidation activity of Au–Pd alloy NPs does not evolve linearly with their overall chemical composition. In particular, $T_{1/2}$ for Au₉Pd₉₁ NPs $\sim T_{1/2}$ for Au₄₅Pd₅₅ NPs $< T_{1/2}$ for Au₆₉Pd₃₁ NPs $< T_{1/2}$ for pure Au NPs. Evidently, intermixing of a less reactive metal (Au) with a more reactive metal (Pd) in the range of Au:Pd ratios from about 10% to 50% results in nanoalloys whose

catalytic properties, in particular CO oxidation activity, are beyond those of the individual constituents. The specific surface structural features of Au–Pd alloy NPs behind the unusual plateau- and not volcano-type dependence of their catalytic activity on the relative ratio of individual (Au and Pd) constituents are revealed by resonant HE-XRD described below.

The surface atomic structure of pure Au and $\text{Au}_x\text{Pd}_{100-x}$ alloy NPs ($x = 9, 45, \text{ and } 69$) was determined by resonant HE-XRD carried out at the K absorption edges of Au (80.725 keV) and Pd (24.347 keV) coupled to analysis of the experimental data in terms of element-specific atomic PDFs. Details of the resonant HE-XRD experiments and derivation of element-specific atomic PDFs are given in the Methods section of the [Supporting Information](#). Exemplary HE-XRD patterns are shown in [Figure S5](#) (left). As can be seen in the figure, HE-XRD patterns for $\text{Au}_x\text{Pd}_{100-x}$ alloy NPs ($x = 9, 45, 69, \text{ and } 100$) exhibit a few broad, Bragg-like peaks at low diffraction angles and discernible physical oscillations at high diffraction angles, a picture typical for nanocrystalline materials.^{35–38} The diffuse character of the HE-XRD patterns though renders sharp Bragg peak based procedures for determining the atomic structure of bulk (polycrystalline) metals and alloys difficult to apply to the NPs studied here. However, as data in [Figure 2](#) and [Figure S5](#) (right) show, the Fourier transforms of the HE-XRD patterns, known as total PDFs $G(r)$, exhibit a sequence of distinct peaks at high- r values and so lend themselves to convenient testing,

refining, and ultimately determining the complete atomic structure of the NPs, including the NP surface.

By definition, the PDF $G(r) = 4\pi r(\rho(r) - \rho_o)$, where $\rho(r)$ and $\rho_o = \text{const} \neq 0$ are the local and average atomic number density of the material studied, respectively. Hence, experimental $G(r)$ s always oscillate about zero and peak at distances where the local atomic density is larger than the average one, that is, at distances between pairs of atoms, immediate and all farther neighbors, within the metallic NPs studied. The area under the peaks is proportional to the number of atomic pairs at those distances.^{35–38} Since surface atoms at the opposite sides of metallic NPs are separated the most, experimental $G(r)$ s may show distinct peaks at distances extending up to the average NP size only, as demonstrated in [Figure 2](#) (left). Naturally, peaks at these higher- r distances may reflect correlations between atoms near the NP surface alone. Hence, atomic PDFs obtained through HE-XRD, in particular their higher- r peaks, are sensitive to the relative positioning and number of surface atoms in metallic NPs. Indeed, this may not come as a surprise since atoms at the surface of metallic NPs constitute a very substantial fraction of the overall volume of the NPs and XRD is known to be sensitive to the volume fraction of the constituents of any metallic material down to a few %.³⁷ To be more precise, atoms forming the two outermost layers of pure Au and $\text{Au}_x\text{Pd}_{100-x}$ alloy NPs ($x = 9, 45, \text{ and } 69$) are about 35% of all atoms in the NPs. The inherent sensitivity of atomic PDFs to the surface atomic structure of metallic NPs is advantageous to the ongoing effort to develop affordable and efficient nanoalloy catalysts for practical applications. That is because it is the surface of metallic NPs where chemical reactions take place.

To ascertain the structure type of $\text{Au}_x\text{Pd}_{100-x}$ alloy NPs ($x = 9, 45, 69, \text{ and } 100$), the experimental total atomic PDFs were approached with a simplistic model constrained to an fcc-type crystal structure. The model made sense since bulk Au, Pd, and Au–Pd alloys are fcc-type crystals. Details of the computations are given in the Methods section of the [Supporting Information](#). Results from the computations are shown in [Figure 2](#) (right). As can be seen in the figure, largely, the NPs maintain the fcc-type structure exhibited by their bulk counterparts. However, contrary to the case of bulk Au–Pd alloys, the “fcc-lattice” parameter for $\text{Au}_x\text{Pd}_{100-x}$ alloy NPs ($x = 9, 45, 69, \text{ and } 100$) does not obey the so-called Vegard’s law envisioning a steady linear change in the lattice parameter for continuous binary alloys in which the two types of distinct atomic species simply substitute for one another.^{32,39} The observation indicates that Au and Pd atoms in $\text{Au}_x\text{Pd}_{100-x}$ alloy NPs ($x = 9, 45, \text{ and } 69$) interact strongly and so arrange in a nonuniform manner.

Despite being informative, an atomic PDF for metallic alloy NPs obtained by a single HE-XRD experiment may not reveal well the mutual arrangement of distinct atomic species in the NPs. That is because such a PDF is a weighted sum of $n(n + 1)/2$ partial PDFs, where n is the number of distinct atomic species in the NPs.^{36,37,40,41} In particular, each of the experimental total PDFs shown in [Figures 2](#) and [S5](#) (right) is a weighted sum of Au–Au, Au–Pd, and Pd–Pd partial PDFs. As elaborated in the Methods section of the [Supporting Information](#) and exemplified in [Figure 3](#), resonant HE-XRD allows resolving the individual partial PDFs for metallic alloy NPs, thereby making it possible to determine precisely the positioning of distinct atomic species throughout the NPs. For example, as data in [Figure 3](#) (left) and [Figure 4b,c](#) show,

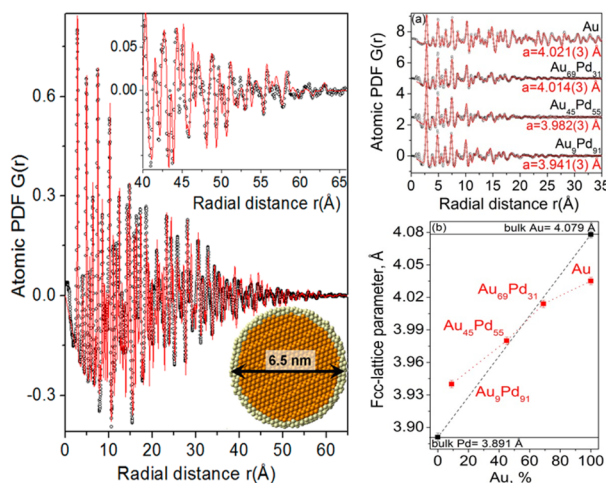


Figure 2. (left) Experimental (symbols) and computed (red line) total PDF for 6.5 nm pure Au particles. The higher- r part of the experimental and computed data is given in the inset. The computed PDF is derived from the respective 3D structure shown in [Figure 4a](#). A 2D cut through the central part of the 3D structure is shown in the lower right corner. The highlighted outer portion of the 2D cut is representative of the two outermost layers of the 3D structure involving about 35% of all (9600) Au atoms in it. (right) (a) Experimental (symbols) and computed (red line) total PDFs for $\text{Au}_x\text{Pd}_{100-x}$ alloy NPs ($x = 9, 45, 69, \text{ and } 100$) NPs. The computed PDFs are based on a model constrained to an fcc-type infinite lattice as explained in the text. Refined “fcc-lattice parameters” are given for each data set. (b) Refined “fcc-lattice parameters” from panel (a) vs the overall composition of the respective NPs. Diagonal broken line (in black) represents the linear (Vegard’s law type) dependence of the fcc-lattice parameter for bulk Au–Pd alloys on their composition, as observed by experiment.³⁹ For comparison, the lattice parameters for bulk fcc Au and Pd metals are also shown at the top and bottom parts of the plot, respectively. Broken line in red is a guide to the eye.

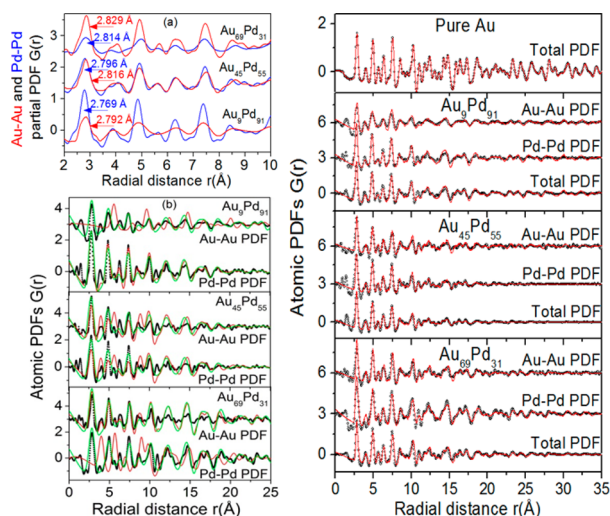


Figure 3. (left) (a) Experimental Au–Au (red line) and Pd–Pd (blue line) partial PDFs for $\text{Au}_x\text{Pd}_{100-x}$ alloy NPs ($x = 9, 45, 69$). Arrows mark the position of the first PDF peak. (b) Experimental (symbols) and computed (lines) Au–Au and Pd–Pd partial PDFs for $\text{Au}_x\text{Pd}_{100-x}$ alloy NPs ($x = 9, 45, 69$). The computed PDFs are derived from the fully chemically ordered (red line) and disordered (green line) 3D atomic configurations shown in Figures 4b and 4c, respectively. (right) RMC fits (red lines) to the experimental (symbols) total and Au–Au and Pd–Pd partial PDFs for $\text{Au}_x\text{Pd}_{100-x}$ alloy NPs ($x = 9, 45, 69, 100$). The fits reflect the respective 3D structures shown in Figure 4a. The goodness-of-fit indicators R_w , defined in the Methods section of the Supporting Information, for the RMC fits are on the order of $11(\pm 2)\%$.

experimental Au–Au and Pd–Pd partial PDFs allow an unambiguous discrimination between competing chemically fully ordered and disordered full-scale atomic configurations for Au–Pd alloy NPs. Furthermore, as demonstrated in Figures S6, S9, S10, and S13, experimental Au–Au and Pd–Pd partial PDFs are very sensitive to the chemical pattern and geometry of the surface of Au–Pd alloy NPs as well as to their shape.

The complete atomic structure of $\text{Au}_x\text{Pd}_{100-x}$ alloy NPs ($x = 9, 45, 69$) was determined strictly adhering to the successful practices of structure studies on polycrystalline metallic materials. From a methodological point of view, this made perfect sense because determining the atomic structure of both polycrystalline and nanocrystalline metallic particles relies on diffraction data obtained from ensembles of entities with a fairly close chemical composition, size, and shape.^{28,42} In brief, full-scale model structures for each of the $\text{Au}_x\text{Pd}_{100-x}$ alloy NPs ($x = 9, 45, 69$, and 100) were generated accounting for the findings of ICP-AES, HR-TEM, and HAADF-STM experiments, that is, the structures featured atomic configurations with the overall (bulk) chemical composition, size (6.5 nm), and shape (polyhedral) of the NPs modeled. Also, as suggested by the findings of crystallography-constrained computations described above, Au and Pd atoms (~ 9600 in total) in the configurations were arranged in an fcc-like manner. Configurations of various chemical patterns were considered. The energy of the configurations was minimized by Molecular Dynamics (MD) simulations based on the quantum-corrected Sutton–Chen potential.^{43–45} Exemplary MD optimized model structures are shown in Figure S6. Best MD-optimized atomic configurations were refined further by hybrid RMC guided by the respective total and Au–Au and Pd–Pd partial PDFs. The refinement was necessary since actual metallic NPs can exhibit surface

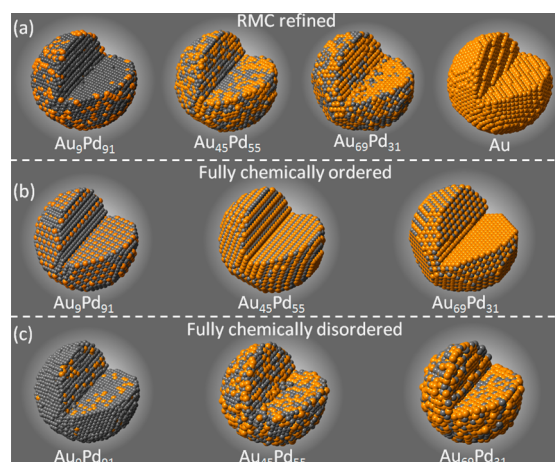


Figure 4. (a) 3D structures for pure Au and $\text{Au}_x\text{Pd}_{100-x}$ alloy NPs ($x = 9, 45, 69$) determined as described in the text. The very good agreement between the partial and total PDFs computed from the structures and those obtained by resonant HE-XRD experiments is demonstrated in Figure 3 (right). (b, c) 3D model structures for $\text{Au}_x\text{Pd}_{100-x}$ alloy NPs ($x = 9, 45, 69$) failing to reproduce the experimental PDF data as demonstrated in Figure 3b (left). Models for $\text{Au}_9\text{Pd}_{91}$ alloy NPs feature a fully chemically ordered (Pearson symbol $tI18$; space group $I4/mmm$) and disordered (Pearson symbol $cF4$; space group $Fm3m$) A_1B_8 -type structure. Models for $\text{Au}_{45}\text{Pd}_{55}$ alloy NPs feature a fully chemically ordered (Pearson symbol $tP4$; space group $P4/mmm$) and disordered (Pearson symbol $cF4$; space group $Fm3m$) AB -type structure. Models for $\text{Au}_{69}\text{Pd}_{31}$ alloy NPs feature a fully chemically ordered (Pearson symbol $cP4$; space group $Pm3m$) and disordered (Pearson symbol $cF4$; space group $Fm3m$) A_3B -type structure. The structures occur, or are likely to occur, with bulk Au–Pd alloys as described in ref 60. Au atoms are in orange, and Pd atoms are in gray.

reconstruction and chemical ordering which may not be captured by MD alone, i.e., without experimental input.^{35,38} As it should be, the thermal (Debye–Waller type) and static displacements, i.e., relaxation, of atoms in the refined configurations were treated separately.^{46,47} More details of the MD and hybrid RMC computations can be found in the Methods section of the Supporting Information.

3. DISCUSSION

The RMC refined full-scale atomic configurations for pure Au and $\text{Au}_x\text{Pd}_{100-x}$ alloy NPs ($x = 9, 45, 69$) are shown in Figure 4a. The configurations are with a realistic size, shape, and overall chemical composition. Besides, they are optimized in terms of energy and, as demonstrated in Figure 3 (right), reproduce very well the respective total and element-specific PDF data. Fine features of the configurations, including the geometry and chemical pattern of their surface, are verified as exemplified in Figures S6, S9, and S10. Moreover, the near surface chemical composition of $\text{Au}_x\text{Pd}_{100-x}$ alloy NPs ($x = 9, 45, 69$) obtained from the configurations (see ref S63) appeared as “ $\text{Au}_{22}\text{Pd}_{78}$ ”, “ $\text{Au}_{47}\text{Pd}_{53}$ ”, and “ $\text{Au}_{60}\text{Pd}_{40}$ ”, respectively, i.e., pretty close to the findings of independent XPS experiments. As such, and in full compliance with the criteria for assessment of the quality of 3D atomic structure determination,^{1,36,40,42,47} the configurations can be considered as the most likely atomic structure of the NPs studied here, including their surface atomic structure. Indeed, the surface and bulk atomic structure of metallic alloy NPs (<10 nm) are likely to be related to each other, if not interwoven, and, for the sake

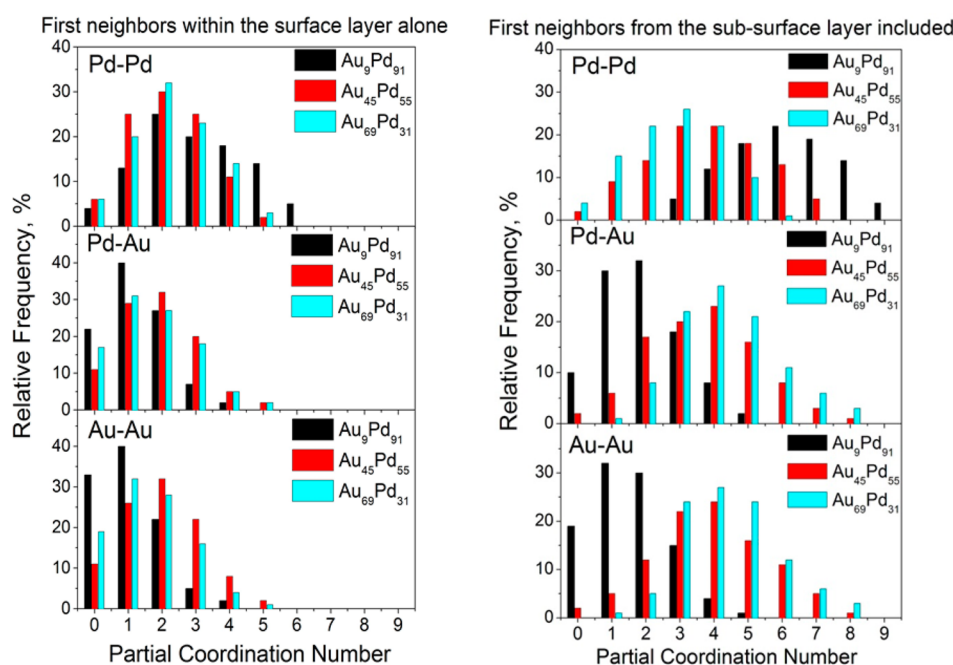


Figure 5. (left) Distribution of partial coordination numbers (CNs) for surface atoms in 6.5 nm $\text{Au}_x\text{Pd}_{100-x}$ alloy NPs ($x = 9, 45, 69$) as extracted from the respective 3D structures shown in Figure 4a. Note that the distribution includes atoms from the top surface layer alone. On average, surface atoms in the NPs studied here may have up to 4.4(1) such neighbors. For comparison, atoms at the (111) surface of bulk fcc metals and alloys have 6 first neighbors from the same close packed surface layer. (right) Distribution of partial CNs for surface atoms in 6.5 nm $\text{Au}_x\text{Pd}_{100-x}$ alloy NPs ($x = 9, 45, 69$) including first neighbors from both the top surface and subsurface layer. On average, surface atoms in the NPs studied here may have up to 7.4(1) such neighbors. For comparison, the total CN for atoms at the (111) surface of bulk fcc metals and alloys is 9 (6 from the same close packed surface layer and 3 from the layer beneath it).

of consistency, ought to be refined together. Here it may be added that describing the structure of binary metal alloys in terms of a large size atomic configurators is not a rarity. For example, the monoclinic (space group C2) $\text{YbCu}_{4.5}$ alloy is described by a 7448-atom unit cell determined by XRD.⁴⁸ Then, in traditional crystallographic terms, $\text{Au}_x\text{Pd}_{100-x}$ alloy NPs ($x = 9, 45, 69$, and 100) can be considered as triclinic (space group P1) nanocrystallites each described by a 9600-atom unit cell. The nanocrystallites though are not piled up together in bulk powder (see TEM images in Figure S1) but are dispersed on fine carbon support, thus becoming an integral part of a typical composite material. This does not preclude determining their 3D structure with high precision.

Using the (x,y,z) coordinates for Au and Pd atoms forming the top two layers of the 3D structures shown in Figure 4a, we derived structural characteristics of prime importance to the catalytic functionality of $\text{Au}_x\text{Pd}_{100-x}$ alloy NPs ($x = 9, 45, 69$), including the total surface coordination numbers (CNs), partials CNs, and bonding distances. Those are directly related to the geometry, chemical pattern, and electronic structure of the NP surface, respectively. Results are summarized in Figure S11 and Figures 5 and 6.

As data in Figure S11 show, the distribution of total surface CNs in pure Au and $\text{Au}_x\text{Pd}_{100-x}$ alloy NPs ($x = 9, 45, 69$) is broad, exhibiting a considerable number of 9- and 8-fold coordinated atoms, indicative of close packed, planar-type atomic configurations; 7- and 6-fold coordinated atoms, indicative of steps and kinks; and a small number of 5- and 4-fold coordinated atoms, indicative of sharp corners at the NP surface. Though coexisting, the configurations are well-defined, as data in Figure 7 show.

As data in Figure 5 show, most ($\sim 70\%$) surface Pd atoms in $\text{Au}_x\text{Pd}_{100-x}$ alloy NPs ($x = 9, 45, 69$) have either one or two unlike (Au) atoms from the same surface layer as first neighbors. Notably, in line with the findings of experiments on model Au–Pd surfaces,^{26,49} at least 5% of all surface Pd atoms appear as monomers, regardless of the overall chemical composition of the NPs. Besides, surface Pd monomers always appear outnumbered by lone surface Au atoms. Altogether, elemental maps, XPS, and data in Figure 5 obtained by resonant HE-XRD and atomic PDF analysis indicate that the surface and overall (bulk) composition of $\text{Au}_x\text{Pd}_{100-x}$ alloy NPs ($x = 9, 45, 69$) are persistently different over a broad range of relative ratios of Au and Pd constituents.

As data in Figure 6 show, on average, surface Au–Au and Pd–Pd bonding distances in $\text{Au}_x\text{Pd}_{100-x}$ alloy NPs ($x = 9, 45, 69$) change significantly and by reciprocal factors with the overall composition of the NPs. Though not exhibited by bulk Au–Pd alloys, the observed systematic change in the bonding distances between like surface atoms, i.e., in the size of surface Au and Pd atoms, may not come as a surprise. According to the theory of chemical bonding of Pauling and independent experimental studies, the elemental size of metal atoms may change upon alloying so that the ratio of the size of the alloyed atoms becomes as close to one as possible, for minimizing atomic level stresses. Furthermore, the theory postulates and experiments confirm that changes in metal-to-metal atom bond lengths trigger changes in both the strength of the respective bonds and the electronic structure of the metal atoms involved in the bonds, and vice versa. That is, the former and the latter indeed occur concurrently as integral parts of the process of minimizing the total energy, i.e., maximizing the stability, of the respective alloys.^{50–54} For metallic alloy NPs in the size range

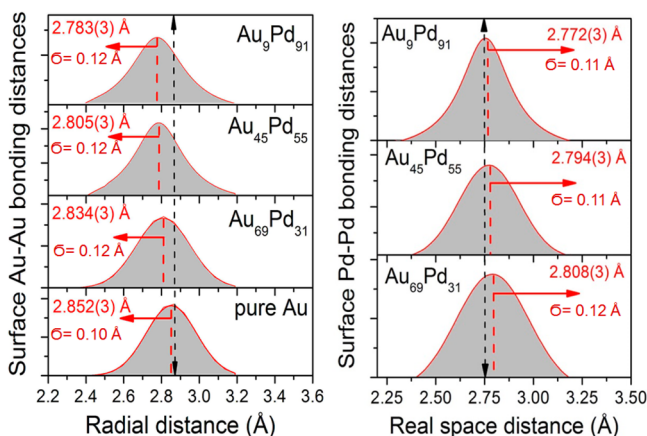


Figure 6. Distribution of surface Au–Au (left) and Pd–Pd (right) bonding distances (gray areas) in pure Au and Au_xPd_{100-x} alloy NPs ($x = 9, 45, 69$) as extracted from the respective 3D structures shown in Figure 4a. The centroid of the distributions, i.e., the average surface Au–Au and Pd–Pd bonding distances, and the average magnitude of the static displacements, σ_s , of surface Au and Pd atoms from their average position are shown for each data set. Note, $\sigma_s = \text{fwhm}/(2\sqrt{2 \ln 2})$, where fwhm is the full width at the half-maximum of the respective distribution of bonding distances as approximated with a Gaussian function (red solid lines). Vertical broken lines in black mark Au–Au (2.875 Å) and Pd–Pd (2.755 Å) bonding distances in bulk Au and Pd, respectively. Vertical broken lines and horizontal arrows in red emphasize the systematic contraction and expansion of surface Au–Au and Pd–Pd bonding distances, i.e., relaxation of surface Au and Pd atoms, with the relative amount of unlike atomic species in the NPs. Note, as expected, the surface and bulk averaged Au–Au and Pd–Pd bonding distances in Au–Pd alloy NPs are not quite the same (compare data presented here and in Figure 3, left).

of a few nanometers, such as Au–Pd alloy NPs studied here, it is not the energy (enthalpy) of formation of the respective alloy that alone determines the stability of their near-surface region, typically comprising the top surface atomic layer and up to 2–3 atomic layers beneath it. Rather, it is the free energy which, besides the alloy formation energy, includes substantial contributions from the usual for metallic NP surface tension, stresses induced by the intermixing of Au and Pd atoms, surface energy of Au and Pd atoms, and interactions with the substrate. The latter may be considered nearly negligible because of the inert nature of the carbon support used here. Besides, within the limits of the experimental accuracy, HE-XRD did not detect metal–carbon or other bonds of nonmetallic character. It is well-known that the enthalpy of mixing of Au and Pd atoms is strongly negative (e.g., -8.4 kJ/mol for Au to Pd ratio of 1:1) and the surface energy of Au (1.62 J/m²) is lower than that of Pd (2.04 J/m²). Furthermore, it is well-known that the elemental size of Au and Pd atoms, i.e., Au–Au and Pd–Pd bonding distances in the respective metals, is 2.875 and 2.755 Å, respectively. Evidently, the minimization of total energy/maximization of thermodynamic stability of Au–Pd alloy NPs occurring during their synthesis and postsynthesis treatment, including the minimization of free surface energy, leads to both the formation of specific surface atomic configurations, such as Au and Pd monomers (like atom CN = 0), dimers (like atom CN = 1), trimers (like atom CN = 2), etc. (see Figures 5 and S11), and a significant relaxation of distinct surface atoms. The latter involves a correlated “compression” and “expansion” of surface Au and Pd atoms, respectively, as compared to their elemental size. The surface electronic structure of Au–Pd alloy

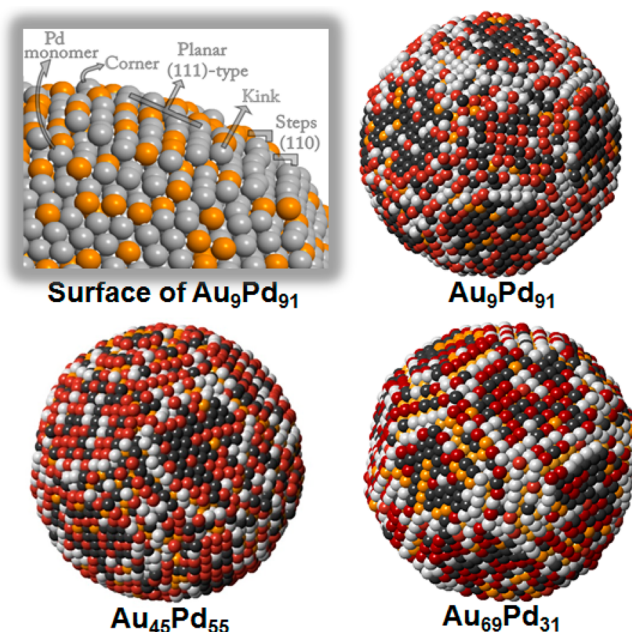


Figure 7. (first row on the left) Fragment from the surface of Au₉Pd₉₁ NPs as revealed by the respective 3D structure shown in Figure 4a. Arrows indicate atoms occupying dense packed (111)-type terraces (total CN = 9), (110)-related steps (total CN = 7 or 8), kinks (total CN = 6), and corners (total CN = 4 or 5). Au atoms are in yellow, and Pd atoms are in gray. (first row on the right and second row) Maps indicating the CO oxidation activity of surface Au and Pd sites in Au_xPd_{100-x} alloy NPs ($x = 9, 45, 69$) as measured by the energy position of the upper edge of the d-band, ϵ_{wd} for the sites. In particular, surface Au atoms whose ϵ_{wd} is lower than that of Au atoms at the (111) surface of bulk Au are shown in yellow. Surface Pd atoms whose ϵ_{wd} is higher than that of Pd atoms at the (111) surface of bulk Pd are shown in gray. According to the refined version of d-band center theory described in refs 76 and 77, such surface Au and Pd atoms are unlikely to contribute to the superb catalytic activity of Au–Pd alloy NPs for CO oxidation. Au atoms whose ϵ_{wd} is shifted upward as compared to the ϵ_{wd} for Au atoms at the (111) surface of bulk Au are shown in red. Surface Pd atoms whose ϵ_{wd} is shifted downward with respect to the ϵ_{wd} for Pd atoms at the (111) surface of bulk Pd are shown in black. According to the refined version of the d-band center theory, these atoms would contribute the most to the superb catalytic activity of Au–Pd alloy NPs for CO oxidation reaction.

NPs, in particular the distribution of valence electron density around the relaxed surface Au and Pd atoms, would change accordingly. Here it is to be underlined that XRD is very suitable for studying changes in the surface electronic structure of metallic NPs because X-rays are scattered by the electron cloud surrounding the nuclei of metal atoms and, as discussed above, the surface of metallic NPs incorporates a very substantial fraction of all atoms in the NPs ($\sim 35\%$ of all atoms in Au_xPd_{100-x} alloy NPs ($x = 9, 45, 69$); see Figure 2). Besides, typically, atomic PDFs reflect diffraction data from $q \sim 0.3$ Å⁻¹ to about 25 Å⁻¹, if not higher, where q is the wave vector (see eqs S1–S3). Diffraction data at low (e.g., <10 Å⁻¹) and relatively high (e.g., ~ 10 Å⁻¹ to 25 Å⁻¹) q -values are particularly sensitive, respectively, to the valence (higher-shell) and tightly bound (inner-shell) electrons of TMs such as Pd and Au.^{55,56} For reference, the valence electrons of Pd($4d^{9.4}5s^{0.6}$) and Au($5d^{9.6}6s^{0.4}$) are about 21% and 14% of all electrons in the respective atoms and so make a substantial

contribution to the diffracted X-ray intensities used in the derivation of atomic PDFs shown in Figure 3 (right).

Often, the size of a metal atom is considered in terms of its elemental Wigner–Seitz radius, r_{ws} , defined as the radius of a sphere whose volume, V_{ws} , is equal to the volume of the so-called Wigner–Seitz (WS) cell occupied by the atom while in the respective solid. In the case of N metal atoms in a volume V of the solid, the Wigner–Seitz radius is defined as $\left(\frac{4}{3}\right)\pi(r_{\text{ws}})^3 = V/N$. Solving for r_{ws} it can be obtained that $r_{\text{ws}} = \left(\frac{3}{4\pi n(r)}\right)^{1/3}$, where $n(r)$ is the average valence electron density of the atom.^{50–52,57,58} Hence, from a local perspective, the size of a metal atom can be related to the spatial extent of the highest energy occupied valence electron orbitals in the atom.^{50,59} For reference, when expressed in atomic number density units, the r_{ws} for Au and Pd atoms in bulk Au and Pd metals is 1.590 and 1.522 Å, respectively.⁵¹

Within the common formalism of WS cells, it may be expected that, when the size of a late-TM atom, A , changes, as measured by the change in the respective bonding distance, d_{AA} , the Wigner–Seitz volume ($V_{\text{ws}}^A = \frac{\sqrt{2}}{2}d_{\text{AA}}^3$ for atoms arranged in a fcc-type manner) and so the average valence electron density for that atom would change, and vice versa.^{54,57–59} As data in Figure 6 show, on average, surface Au–Au bonding distances in pure Au NPs are contracted as compared to the bulk value of 2.875 Å and so, on average, the r_{ws} for surface atoms in pure Au NPs appears reduced to 1.576 Å. The further systematic decrease in the r_{ws} for surface Au atoms in $\text{Au}_x\text{Pd}_{100-x}$ alloy NPs from 1.566 Å for $x = 69$ to 1.550 Å for $x = 45$ and then to 1.538 Å for $x = 9$ indicates that, on average, the valence electron density on surface Au sites in the NPs gradually increases with the relative Pd content. On the other hand, the systematic increase in the average r_{ws} for surface Pd atoms in $\text{Au}_x\text{Pd}_{100-x}$ alloy NPs from 1.532 Å for $x = 9$ to 1.544 Å for $x = 45$ and then to 1.552 Å for $x = 69$ (see Figure 6) indicates that, on average, the valence electron density on surface Pd sites in the NPs gradually decreases with the relative Au content. The concurrent increase and decrease in the valence electron density on surface Au and Pd sites in Au–Pd alloy NPs with the relative content of unlike atomic species may be regarded as an evolving partial negative and positive charge on the respective sites. The evolution of partial charge may include a “charge transfer” between surface atoms, change in the character of valence electrons of surface atoms through $sp-d$ (re)hybridization, and filling and emptying of d-bands and shifts in the energy position of d-bands of surface Au and Pd atoms. Typically, charge is transferred from metal atoms with higher value of Fermi energy toward metal atoms with lower value of Fermi energy. The Fermi energy of metal Au and Pd is 7.25 and 7.69 eV, respectively, as computed using the linear muffin-tin orbital method.^{60,61} Hence, it may be expected that charge will flow from surface Pd \rightarrow surface Au sites, i.e., surface Pd atoms will behave like valence electron donors while surface Au atoms will act as valence electron acceptors. Thus, increasingly, surface Pd sites will be depleted of charge while surface Au sites will acquire extra charge with the increase in the percentage of unlike species in the NPs, as indeed observed here. Note, Pd \rightarrow Au “charge flow” referred to above does not imply actual transfer of electrons onto surface Au sites. Rather, it envisages a shift of charge from the inner toward the outer portion of the “expanded” WS cells for surface Pd atoms, and

vice versa for the shift of charge within the “compressed” WS cells for surface Au atoms, leading to an equilibration of the initially different valence electron density/Fermi levels of the respective atoms.^{25,62,63} The magnitude of the observed reciprocal changes in the r_{ws} for surface Au and Pd atoms indicates that the highly correlated shift of charge within their WS cells may involve up to 0.3(1) valence electrons. Though small and very much local, that shift of charge may change significantly the character of valence electrons near the Fermi level in the vicinity of surface Au and Pd sites in Au–Pd alloy NPs and, hence, significantly affect the reactivity of the NPs.

In particular, considering the fact that the WS cells for surface Pd atoms and Au atoms in Au–Pd alloy NPs appear “expanded” and “compressed”, respectively, it may be conjectured that the atoms gain and lose electrons occupying their most spatially extended orbitals, respectively. To be more specific, considering the decrease in the surface Au–Au bonding distances, i.e., increased d–d electron interactions, it may be conjectured that 6sp electrons of surface Au atoms gain more 5d-character through $sp \rightarrow d$ charge redistribution (rehybridization) and so the valence electronic configuration of the atoms increasingly becomes more $5d^{10}6s^1$ -like (vs $5d^96s^2(sp)^{1.4}$ bulk configuration) with the increase in the concentration of Pd in the NPs. Effectively, both the increased d-charge density and decreased Au–Au bonding distances (d orbital–d orbital separation) would widen the 5d-band of surface Au atoms pushing its top closer to the Fermi level. Ultimately, this would increase the reactivity of surface Au atoms in Au–Pd alloy NPs, as compared to corresponding atoms on the surface of pure Au NPs.^{60,63–67} This scenario is in line with the changes in the intensity of the so-called Au L_3 line regarded as a signature of the presence of vacancies (d-holes) in the valence 5d-band of Au atoms. As found by EXAFS, the line decays gradually with the concentration of Pd atoms in Au–Pd alloy NPs and virtually disappears when that concentration approaches 80%.³¹ On the other hand, considering the increase in the average surface Pd–Pd bonding distances, i.e., weakened d–d electron interactions, it may be conjectured that the 5sp electrons of surface Pd atoms lose some d-character. Alternatively, the increased degree of delocalization of charge on surface Pd sites in Au–Pd NPs may be looked at merely as a “dilation” of the charge due to the “expanded” WS cells for the atoms occupying the sites. The decreased charge density and increased Pd–Pd bonding distances (d orbital–d orbital separation) would narrow the 4d-band of surface Pd sites effectively pushing its top below the Fermi level. Ultimately, this would render surface Pd atoms in Au–Pd alloy NPs less reactive, as compared to corresponding atoms on the surface of pure Pd NPs.^{12–14,68–70} This scenario is supported by scanning tunneling microscopy studies on Pd atoms deposited on monolayers of pure Au. In particular, the studies have found that even when completely isolated the former bear a partial positive charge while nearby Au atoms are somewhat electron-rich.⁶⁸

The concurrent reciprocal changes in the reactivity of surface Au and Pd atoms would affect the CO oxidation activity of Au–Pd alloy NPs very significantly.^{12,70–74} In particular, usually, the CO oxidation reaction proceeds through the so-called Langmuir–Hinshelwood mechanism, that is, CO molecules adsorbed onto a catalyst surface react with nearby adsorbed oxygen species to form CO_2 . For clarity, the reaction path can be divided into four steps as follows: $\text{CO}_{(\text{gas})} + * \rightarrow \text{CO}^* (1)$; $\text{O}_{2(\text{gas})} + * \rightarrow \text{O}_2^* (2)$; $\text{O}_2^* + * \rightarrow \text{O}^* + \text{O}^* (3)$; $\text{CO}^* + \text{O}^*$

→ CO_{2(gas)} + * + * (4), where “*” stands for a surface atomic site capable of binding CO or oxygen species. Pure Pd NPs bind CO molecules and oxygen species (steps 1, 2, and 3 above) strongly, i.e., exhibit high catalytic activity for CO oxidation reaction. Under typical reaction conditions though, the surface of Pd NPs may end up irreversibly covered (“poisoned”) with reactants and reaction intermediates. Hence, the rate of CO oxidation over pure Pd NPs, in particular step (4) of the reaction, would be limited.^{20–22} Pure Au NPs bind CO and particularly oxygen species much less strongly than Pd NPs do.^{3,4,13} Hence, the low probability of adsorption of reactants and particularly high energy barrier for dissociation (activation) of molecular oxygen (O₂), that is, step (3) of the reaction, would limit the rate of CO oxidation over pure Au NPs. Note, it is considered that activation barriers for a surface reaction, such as, for example, dissociation of O₂, would follow the trends of adsorption energies, that is, a change in the adsorption energy of oxygen species at a surface site would change the energy barrier for O₂ dissociation at that site.^{12,14,20,21}

On a molecular level, the adsorption of a CO molecule on an active surface site may be considered in terms of concurrent transfers of charge from the filled 2σ-orbital of the molecule to the surface site (donation) and d-charge from the surface site into vacant 2π*-orbitals of the molecule (back-donation). On the other hand, the adsorption of O₂ on an active surface site may be considered in terms of concurrent transfer of charge from the occupied π-bonding orbital of the molecule to the surface site (σ-donor interaction) and d-charge from the surface site into empty π*-orbitals of the molecule (π-acceptor interaction). Then, as discussed in prior studies,^{12–14} the decrease in the d-electron DOS in the vicinity of surface Pd sites in Au–Pd NPs would reduce the transfer of d-charge into the 2π*-orbitals of CO molecules and π*-orbitals of O₂ molecules adsorbed onto the sites. This would reduce both the CO and O₂ adsorption energy at the sites, thereby significantly reducing the likelihood of surface Pd sites getting poisoned during the CO oxidation reaction. On the other hand, the increase in the d-electron DOS in the vicinity of surface Au sites in Au–Pd alloy NPs would increase the transfer of d-charge into the π*-orbitals of O₂ molecules and 2π*-orbitals of CO molecules adsorbed onto the sites. This would increase both the O₂ and CO adsorption energy at the sites, thereby increasing the probability of populating surface Au sites with reactants. Therefore, according to the concepts considering the local d-DOS at the Fermi energy as a major factor in determining the surface reactivity of alloys based on late TMs, the interrelated increase and decrease in the d-character of DOS at surface Au and Pd atoms, respectively, would amplify each other's positive contributions to the catalytic activity of Au–Pd alloy NPs for CO oxidation reaction. In essence, this may be considered as the hallmark of the catalytic synergy between surface Au and Pd atoms in Au–Pd alloy NPs. Noteworthy, prior studies have also found that the presence of partial negative and positive charge on surface sites in pure Au and Pd NPs, respectively, significantly increases their CO oxidation activity.^{12,20,70–75}

To reveal the structural origin of the catalytic synergy of surface Au and Pd atoms in Au–Pd alloy NPs in better detail, we summarized the surface structure and catalytic data obtained here in Figure 8. As data for T_{1/2} and TOF in Figure 8a clearly show, Au–Pd alloy NPs poor in Au (with 0 < Au% ≤ 50 atomic %) function much better as CO oxidation catalysts in

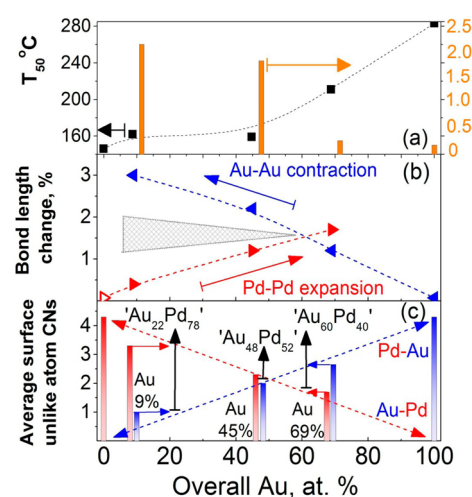


Figure 8. Evolution of the surface structural characteristics and CO oxidation activity for Au_xPd_{100-x} alloy NPs ($x = 9, 45, 69, 100$) with their overall composition, x . (a) Experimental T_{50} (black rectangles) and TOF (orange bars) for CO oxidation reaction. Broken line is a best fit to the data. (b) Relative change in the average surface Au–Au (blue triangles) and Pd–Pd (red triangles) bonding distances as extracted from the respective 3D structures shown in Figure 4a. Broken lines are best fits to the respective data sets. The shaded area indicates the range of Au to Pd ratios within which Au–Pd alloy NPs would outperform pure Pd and Au NPs as catalysts for CO oxidation reaction. (c) Average surface Pd–Au (blue bars) and Au–Pd CNs (red bars) including first neighbors from the same top surface layer alone. Broken lines trace the evolution of Au–Pd and Pd–Au CNs for an Au–Pd surface layer involving as many unlike, i.e., Au–Pd and Pd–Au, atomic pairs as possible given the overall chemical composition of Au–Pd alloy NPs. The layer may be considered as a “skin” on top of Au–Pd alloy NPs as explained in the text. The relationship between the composition of the “skin” and the overall composition of Au–Pd alloy NPs is indicated by horizontal and vertical solid arrows in the respective color.

comparison to Au–Pd alloy NPs rich in Au ($50 < \text{Au} \leq 100$ atom %). As data in Figures 8a, 8b, and 8c show, the CO oxidation activity of Au–Pd alloy NPs is maximized when (i) surface Au atoms are strongly (2 to 3%) “compressed” and so exhibit a partial negative charge, (ii) surface Pd atoms are “expanded” to a certain degree (1 to 2%) and so exhibit some positive charge, and (iii) the percentage of surface Au atoms exceeds the overall percentage of Au atoms in the NPs.

Altogether, data in Figure 8a–c indicate that the catalytic synergy of surface Au and Pd atoms in Au–Pd alloy NPs is related to a very specific structural feature of the surface of Au–Pd alloy NPs, that is, the formation of a specific “skin” on top of the NPs involving as many unlike, i.e., Au–Pd and Pd–Au, atomic pairs as possible given the overall composition of the NPs (follow the arrows in Figure 8c). Others have considered the bonding preference of surface Au and Pd atoms in terms of some Coulomb Pd–Pd repulsion and net charge transfer from Pd to Au.¹² Here we show that unlike atoms from the “skin” indeed interact strongly, including changing their size and electronic structure in inverse proportions, and so endow Au–Pd alloy NPs with a superb catalytic activity for CO oxidation. The strong heteroatomic interactions would definitely impede the migration of individual near-surface Au and Pd atoms through the “skin”, thereby improving the stability of Au–Pd alloy NPs under the conditions of chemical reactions.^{12,20,21}

To assess the consistency of our experimental findings, we exploited a refined version of the d-band center theory on the catalytic properties of TM metals and alloys.^{76,77} In particular, we computed the energy position, ϵ_{wd} , of the upper edge of the d-band for surface Au and Pd atoms in Au–Pd alloy NPs using the $\{x,y,z\}$ coordinates of surface atoms in the respective 3D structures shown in Figure 4a. According to the refined theory, the position can be derived as $\epsilon_{\text{wd}} = \epsilon_{\text{d}} + w_{\text{d}}/2$, where ϵ_{d} and w_{d} are the energy center and width of the d-band, respectively. Using ϵ_{wd} as a descriptor for reactivity made sense since electrons near the top of the d-band are more likely than low lying d-electrons to form bonds with frontier orbitals of reactants such as CO and oxygen molecules. Besides, the values of ϵ_{wd} have been shown to correlate particularly well with the binding energy of oxygen adsorbed on the surface of TMs [see Figure 9 in ref 77]. As discussed above, the strength of binding of oxygen species onto Au and Pd surface sites is an important factor in determining the kinetics of CO oxidation reaction. Details of the calculations are given in the Methods section of the Supporting Information. A map indicative of the catalytic activity of $\text{Au}_x\text{Pd}_{100-x}$ alloy NPs ($x = 9, 45, 69$) for CO oxidation reaction, as measured by the ϵ_{wd} for surface Au and Pd atoms in the NPs, is shown in Figure 7. As can be seen in the figure, a large number of nearby surface Au and Pd atoms would form sites with improved ability to catalyze CO oxidation reactions, as compared to corresponding sites in pure Au and Pd NPs. Besides, many of the sites would involve adjacent short chains of Au and Pd atoms which, as pointed out in the work of others,^{12,20,21,78,79} are essential for the catalytic activity of Au–Pd alloy NPs for CO oxidation and other reactions. Thus, though apparently simplified and accounting for particular steps of the CO oxidation reaction only, theory using experimental surface structure data produced predictions for the catalytic activity of Au–Pd alloy NPs that agree well with independently obtained catalytic data for the same NPs. The agreement testifies to the potential of resonant XRD and element-specific atomic PDF analysis to deliver meaningful surface structure data for metallic NPs of importance to the field of catalysis.

Here it may be noted that, as data sets in Figures 6, 7, and 8a–c indicate, the surface atomic and electronic structure of Au–Pd alloy NPs evolve continuously with the overall composition of the NPs. Hence, for a given bimetallic composition, Au–Pd alloy NPs may appear as a poor catalyst for certain chemical reactions and a highly active one for others, as indeed observed on numerous occasions.^{12,17–21} In particular, “ensemble effects” envisioning Pd monomers (surface Pd–Pd CN = 0) spaced at about 3.3 Å have been considered as a major factor behind the high catalytic activity of Pd-poor Au–Pd nanoalloys for acetoxylation of ethylene to vinyl acetate (VA).¹⁹ According to structure data in Figures 6 and 8, bonding distances between surface Pd atoms in Au–Pd alloy NPs may expand toward 3 Å due to strong interactions with nearby surface Au atoms. Hence, not only Pd monomers but also Pd dimers (Pd–Pd CN = 1) may have to be factored in when the surface structure–catalytic activity relationship in Au–Pd nanoalloy catalyst for VA synthesis is assessed.

Last but not least, it is well-known that theoretical descriptors for the reactivity of TMs and their alloys are very sensitive to fine computational details. This makes the descriptors less useful for understanding and predicting atomic surface structure–reactivity relationships and requires developing of algorithms for estimating the uncertainty of theoretical

predictions, offset corrections, and others.^{80,81} On the other hand, little attention is paid to the fact that, typically, the theory on surface-controlled properties of metallic NPs, in particular the catalytic properties, is applied on 3D periodic slabs of nearly perfect fcc(111), hcp(001), and bcc(110) atomic planes. As shown here and elsewhere,^{35,36,38,40} the facets of real-world metallic NPs are not necessarily perfectly 3D periodic at atomic level. We argue that, among others, the accuracy of theory on the catalytic properties of metallic NPs may be improved by applying the theory on a more realistic atomic-level basis delivered by advanced analytical techniques such as resonant HE-XRD. Given the model size limitations of electronic structure theory, it may be argued that such an approach would be impractical. As we demonstrated recently though, a realistic atomic-level basis for theoretical calculations need not necessarily include the full-scale surface structure determined by experiment. A statistically representative segment of the structure may suffice.⁸² Besides, model size limitations can be overcome by using a simplified theoretical framework such as MD based on interatomic potentials trained against experimental data for the actual surface of metallic NPs under study.³⁸

4. CONCLUSION

The contributions of the surface and interior of metallic NPs to the physicochemical properties of the NPs can differ significantly. Moreover, the former can easily overwhelm the latter, endowing the NPs with a unique functionality. Hence, precise knowledge of the actual surface of metallic NPs is a prerequisite to gaining control over their performance in practical applications, particularly in the field of catalysis. Resonant HE-XRD and element-specific PDF analysis done on metallic NPs synthesized with due care, i.e., as monodisperse in size and chemical composition as possible, can deliver surface structure data relevant to the actual metallic NPs studied, including the relative amount, location in terms of (x,y,z) coordinates, and geometric environment of distinct surface atomic species. It is our belief that such data would help bridge model-surface oriented theory and reality necessitating the production, characterization, and usage of metallic NPs en masse, and thus help design and produce efficient and affordable catalysts for practical applications. Though counter-intuitive, the technique succeeds because (i) atoms at the surface of metallic NPs occupy a very substantial fraction of their overall volume and (ii) XRD is known to be sensitive to the volume fraction of the constituents of any metallic material down to a few % and over a long range of interatomic distances. An added benefit is the capability of the technique to “highlight” surface structural features involving preselected metallic species and “dim” others, thereby revealing the surface atomic structure of metallic NPs with both element specificity and high spatial resolution. In terms of statistics, resonant HE-XRD is as representative of the ensemble of metallic NPs studied as the widely used traditional XRD and EXAFS are. However, when compared to the former, the latter are less sensitive to the surface atomic structure of metallic NPs because, due to their nature, they deliver structure data averaged over the NP volume alone.

■ ASSOCIATED CONTENT

Supporting Information

The Supporting Information is available free of charge on the ACS Publications website at DOI: 10.1021/acs.jpcc.7b00139.

Experimental and computational procedures, TEM images, XRD patterns, XPS spectra, and catalytic data (PDF)

AUTHOR INFORMATION

Corresponding Author

*Tel: +(989) 774 3395. Fax: +(989) 774 2697. E-mail: petko1vg@cmich.edu.

ORCID

Valeri Petkov: 0000-0002-6392-7589

Notes

The authors declare no competing financial interest.

ACKNOWLEDGMENTS

This work was supported by the U.S. Department of Energy (DOE), Office of Science, Basic Energy Sciences, under Grant DE-SC0006877. The research used resources of the Advanced Photon Source, a U.S. Department of Energy (DOE) Office of Science User Facility operated for the DOE Office of Science by Argonne National Laboratory under Contract No. DE-AC02-06CH11357. Thanks are due to staff scientists at the beamlines 1-ID⁸³ and 6-ID at the Advanced Photon Source for the help with resonant HE-XRD experiments.

REFERENCES

- (1) Giacovazzo, C. *Fundamentals of Crystallography*; Oxford University Press: Oxford, U.K., 1992.
- (2) Pearson, W. B. *The crystal chemistry and physics of metals and alloys*; Wiley-INTERSCIENCE: New York, 1972.
- (3) Haruta, M.; Kobayashi, T.; Sano, H.; Yamada, N. Novel Gold Catalysts for the Oxidation of Carbon Monoxide at a Temperature far Below 0 °C. *Chem. Lett.* **1987**, *16*, 405–408.
- (4) Deng, W.; Carpenter, C.; Yi, N.; Flytzani-Stephanopoulos, M. Comparison of the Activity of Au/CeO₂ and Au/Fe₂O₃ Catalysts for the CO Oxidation and the Water-Gas Shift Reactions. *Top. Catal.* **2007**, *44*, 199–208.
- (5) Abad, A.; Concepcion, P.; Corma, A.; Garcia, H. A Collaborative Effect between Gold and a Support Induces the Selective Oxidation of Alcohols. *Angew. Chem., Int. Ed.* **2005**, *44*, 4066–4069.
- (6) Twigg, M. W. Catalytic Control of Emissions from Cars. *Catal. Today* **2011**, *163*, 33–41.
- (7) Baltrus, J. P.; Granite, E. J.; Rupp, E. C.; Stanko, D. C.; Howard, B.; Pennline, H. W. Effect of Palladium Dispersion on the Capture of Toxic Components from Fuel Gas by Palladium-Alumina Sorbents. *Fuel* **2011**, *90*, 1992–1998.
- (8) Gallon, B. J.; Kojima, R. W.; Kaner, R. B.; Diaconescu, P. L. Palladium Nanoparticles Supported on Polyaniline Nanofibers as a Semi-Heterogeneous Catalyst in Water. *Angew. Chem., Int. Ed.* **2007**, *46*, 7251–7254.
- (9) Seechurn, C. C. C. J.; Kitching, M. O.; Colacot, T. J.; Snieckus, V. Palladium-Catalyzed Cross-Coupling: A Historical Contextual Perspective to the 2010 Nobel Prize. *Angew. Chem., Int. Ed.* **2012**, *51*, 5062–5085.
- (10) Wu, X.-F.; Anbarasan, P.; Neumann, H.; Beller, M. From Noble Metal to Nobel Prize: Palladium-Catalyzed Coupling Reactions as Key Methods in Organic Synthesis. *Angew. Chem., Int. Ed.* **2010**, *49*, 9047–9050.
- (11) Mattheiss, L. F.; Dietz, R. E. Relativistic tight-binding calculation of core-valence transitions in Pt and Au. *Phys. Rev. B: Condens. Matter Phys.* **1980**, *22*, 1663–1676.
- (12) Gao, F.; Goodman, D. W. Pd–Au Bimetallic Catalysts: Understanding Alloy Effects from Planar Models and (Supported) Nanoparticles. *Chem. Soc. Rev.* **2012**, *41*, 8009–8020.

(13) Ruban, A.; Hammer, B.; Stoltze, P.; Skriver, H. L.; Norskov, J. Surface Electronic Structure and Reactivity of Transition and Noble Metals. *J. Mol. Catal. A: Chem.* **1997**, *115*, 421–429.

(14) Hammer, B.; Norskov, J. K. Theoretical Surface Science and Catalysis- Calculations and Concepts. *Adv. Catal.* **2000**, *45*, 71–129.

(15) Lopez, N.; Janssens, T. V. W.; Clausen, B. S.; Xu, Y.; Mavrikakis, M.; Bligaard, T.; Norskov, J. K. On the Origin of the Catalytic Activity of Gold Nanoparticles for Low-Temperature CO Oxidation. *J. Catal.* **2004**, *223*, 232–235.

(16) Smith, N. V.; Wertheim, G. K.; Hüfner, S.; Traum, M. M. Photoemission Spectra and Band Structures of d-Band Metals. IV. X-ray Photoemission Spectra and Densities of States in Rh, Pd, Ag, Ir, Pt, and Au. *Phys. Rev. B* **1974**, *10*, 3197–3206.

(17) Enache, D. I.; Edwards, J. K.; Landon, Ph.; Solsona-Espriu, B.; Carley, A. F.; Herzing, A. A.; Watanabe, M.; Kiely, Ch. J.; Knight, D. W.; Hutchings, G. J. Solvent-Free Oxidation of Primary Alcohols to Aldehydes Using Au-Pd/TiO₂ Catalysts. *Science* **2006**, *311*, 362–365.

(18) Kesavan, L.; Tiruvalam, R.; Rahim, M. H. A.; bin Saiman, M. I.; Enache, D. I.; Jenkins, R. K.; Dimitratos, N.; Lopez-Sanchez, J. A.; Taylor, S. H.; Knight, D. W.; Kiely, Ch. J.; Hutchings, G. J. Solvent-Free Oxidation of Primary Carbon-Hydrogen Bonds in Toluene Using Au-Pd Alloy Nanoparticles. *Science* **2011**, *331*, 195–199.

(19) Chen, M.; Kumar, D.; Yi, C.-W.; Goodman, D. W. The Promotional Effect of Gold in Catalysis by Palladium-Gold. *Science* **2005**, *310*, 291–293.

(20) Cuenya, B. R.; Beharid, F. Nanocatalysis: Size- and Shape-Dependent Chemisorption and Catalytic Reactivity. *Surf. Sci. Rep.* **2015**, *70*, 135–187.

(21) Antolini, E. Palladium in Fuel Cell Catalysis. *Energy Environ. Sci.* **2009**, *2*, 915–931.

(22) Ward, T.; Delannoy, L.; Hahn, R.; Kendell, S.; Pursell, Ch. J.; Louis, C.; Chandler, B. D. Effects of Pd on Catalysis by Au: CO Adsorption, CO Oxidation, and Cyclohexene Hydrogenation by Supported Au and Pd–Au Catalysts. *ACS Catal.* **2013**, *3*, 2644–2653.

(23) Klyushin, A. Yu.; Arrigo, R.; Youngmi, Y.; Xie, Z.; Havecker, M.; Bukhtiyarov, A. V.; Prosvirin, I. P.; Bukhtiyarov, V. I.; Knop-Gericke, A.; Schlogl, R. Are Au Nanoparticles on Oxygen-Free Supports Catalytically Active? *Top. Catal.* **2016**, *59*, 469–477.

(24) Note, following the widely adopted definition (e.g., see: Callister, W. D. *Materials Science and Engineering: An Introduction*; John Wiley & Sons: New York, 2007), throughout the paper the term “alloy” is used to describe any mixture of distinct metallic species, irrespective of the degree of their mixing and way of mixing.

(25) Nascente, P. A. P.; de Castro, S. G. C.; Landers, R.; Kleiman, G. G. X-ray Photoemission and Auger Energy Shifts in Some Gold-Palladium Alloys. *Phys. Rev. B: Condens. Matter Phys.* **1991**, *43*, 4659–4666. Lee, Y.-S.; Jeon, Y.; Chung, Y.-D.; Lim, K.-Y.; Whang, C.-N.; Oh, S.-J. Charge Redistribution and Electronic Behavior in Pd–Au Alloys. *J. Korean Phys. Soc.* **2000**, *37*, 451–455.

(26) Yi, C.-W.; Luo, K.; Wei, T.; Goodman, D. W. The Composition and Structure of Pd–Au Surfaces. *J. Phys. Chem. B* **2005**, *109*, 18535–18540.

(27) Coulthard, I.; Degen, S.; Zhu, Y.-J.; Sham, T. K. Gold Nanoclusters Reductively Deposited on Porous Silicon: Morphology and Electronic Structures. *Can. J. Chem.* **1998**, *76*, 1707–1716.

(28) Aruna, I.; Mehta, B. R.; Malhotra, L. K.; Shivaprasad, S. M. Size Dependence of Core and Valence Binding Energies in Pd Nanoparticles: Interplay of Quantum Confinement and Coordination Reduction. *J. Appl. Phys.* **2008**, *104*, 064308.

(29) Richter, B.; Kühlenbeck, H.; Freund, H.-J.; Bagus, P. S. Cluster Core-Level Binding-Energy Shifts: The Role of Lattice Strain. *Phys. Rev. Lett.* **2004**, *93*, 026805.

(30) Sengar, S. K.; Mehta, B. R.; Gupta, G. Charge Transfer, Lattice Distortion, and Quantum Confinement Effects in Pd, Cu, and Pd–Cu Nanoparticles; Size and Alloying Induced Modifications in Binding Energy. *Appl. Phys. Lett.* **2011**, *98*, 193115–3.

(31) Liu, F.; Wechsler, D.; Zhang, P. Alloy-Structure-Dependent Electronic Behavior and Surface Properties of Au–Pd Nanoparticles. *Chem. Phys. Lett.* **2008**, *461*, 254–259.

- (32) Xu, J.; White, T.; Li, P.; He, C.; Yu, J.; Yuan, W.; Han, Y.-F. Biphasic Pd–Au Alloy Catalyst for Low-Temperature CO Oxidation. *J. Am. Chem. Soc.* **2010**, *132*, 10398–10406.
- (33) Venezia, A. M.; Liotta, L. F.; Pantaleo, G.; La Parola, V.; Deganello, G.; Beck, A.; Koppány, Z.; Frey, K.; Horváth, D.; Gucci, L. Activity of SiO₂ Supported Gold-Palladium Catalysts in CO Oxidation. *Appl. Catal., A* **2003**, *251*, 359–368.
- (34) Alayoglu, S.; Tao, F.; Altoe, V.; Specht, C.; Zhu, Z.; Aksoy, F.; Butcher, D. R.; Renzas, R. J.; Liu, Z.; Somorjai, G. A. Surface Composition and Catalytic Evolution of Au_xPd_{1-x} ($x = 0.25, 0.50$ and 0.75) Nanoparticles Under CO/O₂ Reaction in Torr Pressure Regime and at 200 °C. *Catal. Lett.* **2011**, *141*, 633–640.
- (35) Petkov, V. Nanostructure by High-Energy X-ray Diffraction. *Mater. Today* **2008**, *11*, 28–38.
- (36) Petkov, V.; Prasai, B.; Ren, Y.; Shan, S.; Luo, J.; Joseph, P.; Zhong, C. J. Solving the Nanostructure Problem: Exemplified on Metallic Alloy Nanoparticles. *Nanoscale* **2014**, *6*, 10048–10061.
- (37) Klug, P. K.; Alexander, L. E. *X-Ray Diffraction Procedures: For Polycrystalline and Amorphous Materials*; Wiley: New York, 1974.
- (38) Prasai, B.; Wilson, A. R.; Wiley, B. J.; Ren, Y.; Petkov, V. On the Road to Metallic Nanoparticles by Rational Design: Bridging the Gap between Atomic-Level Theoretical Modeling and Reality by Total Scattering Experiments. *Nanoscale* **2015**, *7*, 17902–17922.
- (39) Denton, A. R.; Ashcroft, N. W. Vegard's Law. *Phys. Rev. A: At, Mol, Opt. Phys.* **1991**, *43*, 3161–3163.
- (40) Petkov, V.; Shastri, S. Element-Specific Structure of Materials with Intrinsic Disorder by High-Energy Resonant X-ray Diffraction and Differential Atomic Pair-Distribution Functions: A Study of PtPd Nanosized Catalysts. *Phys. Rev. B: Condens. Matter Mater. Phys.* **2010**, *81*, 165428.
- (41) Petkov, V.; Loukrakpam, R.; Yang, L.; Wanjala, B. N.; Luo, J.; Zhong, C. J.; Shastri, S. Pt–Au Alloying at the Nanoscale. *Nano Lett.* **2012**, *12*, 4289–4299.
- (42) David, W. I. F.; Shakland, K.; McCusker, L. B.; Baerlocher, C. *Structure Determination from Powder Diffraction*; Oxford University Press: Oxford, U.K., 2002.
- (43) Sutton, A. P.; Chen, J. Long-Range Finnis–Sinclair Potentials. *Philos. Mag. Lett.* **1990**, *61*, 139–146.
- (44) Kimura, Y.; Qi, Y.; Cagin, T.; Goddard, W. A., III The Quantum Sutton–Chen Many-body Potential for Properties of fcc Metals. *MRS Symp. Ser.* **1999**, *554*, 43–48.
- (45) Rafii-Tabar, H.; Sulton, A. S. Long-Range Finnis–Sinclair Potentials for f.c.c. Metallic Alloys. *Philos. Mag. Lett.* **1991**, *63*, 217–224.
- (46) Frenkel, A. I.; Machavariani, V. Sh.; Rubshtein, A.; Rosenberg, Yu.; Voronel, A.; Stern, E. A. Local Structure of Disordered Au–Cu and Au–Ag Alloys. *Phys. Rev. B: Condens. Matter Mater. Phys.* **2000**, *62*, 9364–9371.
- (47) Toby, B. H.; Egami, T. Accuracy of Pair Distribution Function Analysis Applied to Crystalline and Non-Crystalline Materials. *Acta Crystallogr., Sect. A: Found. Crystallogr.* **1992**, *48*, 336–346.
- (48) Cerny, R.; Francois, M.; Yvon, K.; Jaccard, D.; Walker, E.; Petricek, V.; Cisarova, I.; Nissen, H.-U.; Wessicken, R. A Single-Crystal X-ray and HRTEM Study of the Heavy-Fermion Compound YbCu_{4.5}. *J. Phys.: Condens. Matter* **1996**, *8*, 4485–4493.
- (49) Wei, T.; Wang, J.; Goodman, D. W. Characterization and Chemical Properties of Pd–Au Alloy Surfaces. *J. Phys. Chem. C* **2007**, *111*, 8781–8788.
- (50) Pauling, L. Factors Determining the Average Atomic Volumes in Intermetallic Compounds. *Proc. Natl. Acad. Sci. U. S. A.* **1987**, *84*, 4754–4756.
- (51) Pauling, L. Electron Transfer in Intermetallic Compounds. *Proc. Natl. Acad. Sci. U. S. A.* **1950**, *36*, 533–538.
- (52) Pauling, L. *The Nature of the Chemical Bond*; Cornell University Press: Ithaca, NY, 1975.
- (53) Rajasekharan, T.; Seshubai, V. Charge Transfer on the Metallic Atom-Pair Bond, and the Crystal Structures Adopted by Intermetallic Compounds. *Acta Crystallogr., Sect. A: Found. Crystallogr.* **2012**, *68*, 156–165.
- (54) Ashcroft, N. W.; Mermin, N. D. *Solid State Physics*; Harcourt College Publishers: 1976.
- (55) Bredtmann, T.; Ivanov, M.; Dixit, G. X-ray imaging of chemically active valence electrons during a pericyclic reaction. *Nat. Commun.* **2014**, *5*, 5589.
- (56) Kissel, L.; Pratt, H. R.; Roy, S. C. Rayleigh scattering by neutral atoms, 100 eV to 10 MeV. *Phys. Rev. A: At, Mol, Opt. Phys.* **1980**, *22*, 1970–2004.
- (57) Watson, R. E.; Hudis, J.; Perlman, M. L. Charge Flow and d Compensation in Gold Alloys. *Phys. Rev. B* **1971**, *4*, 4139–4144.
- (58) Straub, G. K.; Harrison, W. A. Analytic Methods for the Calculation of the Electronic Structure of Solids. *Phys. Rev. B: Condens. Matter Mater. Phys.* **1985**, *31*, 7668–7679.
- (59) Coulthard, I.; Sham, T. K. Charge Redistribution in Pd–Ag Alloys from a Local Perspective. *Phys. Rev. Lett.* **1996**, *77*, 4824–4827.
- (60) Sluiter, M. H. F.; Colinet, C.; Pasturel, A. Ab initio Calculation of the Phase Stability in Au–Pd and Ag–Pt Alloys. *Phys. Rev. B: Condens. Matter Mater. Phys.* **2006**, *73*, 174204.
- (61) Sigalas, M.; Papaconstantopoulos, D. A.; Bacalis, N. C. Total Energy and Band Structure of the 3d, 4d, and 5d Metals. *Phys. Rev. B: Condens. Matter Mater. Phys.* **1992**, *45*, 5777–5783.
- (62) Zhang, P.; Sham, T. K. Tuning the Electronic Behavior of Au Nanoparticles with Capping Molecules. *Appl. Phys. Lett.* **2002**, *81*, 736–738.
- (63) Sun, C. Q. Size dependence of nanostructures: Impact of bond order deficiency. *Prog. Solid State Chem.* **2007**, *35*, 1–159.
- (64) Citrin, P.; Wertheim, G. K.; Baer, Y. Core-Level Binding Energy and Density of States from the Surface Atoms of Gold. *Phys. Rev. Lett.* **1978**, *41*, 1425–1428.
- (65) Jiang, T.; Mowbray, D. J.; Dobrin, S.; Falsig, H.; Bligaard, T.; Norskov, J. K. Trends in CO Oxidation Rates for Metal Nanoparticles and Close-Packed, Stepped, and Kinked Surfaces. *J. Phys. Chem. C* **2009**, *113*, 10548–10553.
- (66) Chou, T. S.; Perlman, M. L.; Watson, R. E. Electronegativity and Electron Binding in Gold Alloys. *Phys. Rev. B* **1976**, *14*, 3248–3250.
- (67) Janssens, V. W.; Clausen, S. B.; Hvolbaek, B.; Falsig, H.; Christensen, C. H.; Bligaard, T. H.; Norskov, J. K. Insights into the reactivity of supported Au nanoparticles: combining theory and experiments. *Top. Catal.* **2007**, *44*, 15–26.
- (68) Baber, A. E.; Tierney, H. L.; Sykes, E. C. H. Atomic-Scale Geometry and Electronic Structure of Catalytically Important Pd/Au Alloys. *ACS Nano* **2010**, *4*, 1637–1645.
- (69) Ontaneda, J.; Bennett, R. A.; Grau-Crespo, R. Electronic Structure of Pd Multilayers on Re(0001): The Role of Charge Transfer. *J. Phys. Chem. C* **2015**, *119*, 23436–23444.
- (70) Rodriguez, J. A.; Goodman, D. W. The Nature of the Metal–Metal Bond in Bimetallic Surfaces. *Science* **1992**, *257*, 897–903.
- (71) Ahmadi, M.; Mistry, H.; Roldan Cuenya, B. Tailoring the Catalytic Properties of Metal Nanoparticles via Support Interactions. *J. Phys. Chem. Lett.* **2016**, *7*, 3519–3533.
- (72) Chen, M.; Cai, Y.; Yan, Z.; Goodman, D. W. On the Origin of the Unique Properties of Supported Au Nanoparticles. *J. Am. Chem. Soc.* **2006**, *128*, 6341–6346.
- (73) Chen, M.; Goodman, D. W. Catalytically Active Gold: From Nanoparticles to Ultrathin Films. *Acc. Chem. Res.* **2006**, *39*, 739–746.
- (74) Kitchin, J. R.; Norskov, J. K.; Barteau, M. A.; Chen, J. G. Modification of the Surface Electronic and Chemical Properties of Pt (111) by Subsurface 3d Transition Metals. *J. Chem. Phys.* **2004**, *120*, 10240–10246.
- (75) Kitchin, J. R.; Norskov, J. K.; Barteau, M. A.; Chen, J. G. Role of Strain and Ligand Effects in the Modification of the Electronic and Chemical Properties of Bimetallic Surfaces. *Phys. Rev. Lett.* **2004**, *93*, 156801.
- (76) Xin, H.; Vojvodic, A.; Voss, J.; Norskov, J. K.; Abild-Pedersen, F. Effects of d-Band Shape on the Surface Reactivity of Transition-Metal Alloys. *Phys. Rev. B: Condens. Matter Mater. Phys.* **2014**, *89*, 115114–5.
- (77) Vojvodic, A.; Norskov, J. K.; Abild-Pedersen, F. Electronic Structure Effects in Transition Metal Surface Chemistry. *Top. Catal.* **2014**, *57*, 25–32.

(78) Gao, F.; Wang, Y.; Goodman, D. W. CO Oxidation over AuPd (100) from Ultrahigh Vacuum to Near-Atmospheric Pressures: The Critical Role of Contiguous Pd Atoms. *J. Am. Chem. Soc.* **2009**, *131*, 5734–5735.

(79) Yu, W.-Y.; Zhang, L.; Mullen, G. M.; Henkelman, G.; Mullins, C. B. Oxygen Activation and Reaction on Pd–Au Bimetallic Surfaces. *J. Phys. Chem. C* **2015**, *119*, 11754–11762.

(80) Deshpande, S.; Kitchin, J. R.; Viswanathan, V. Quantifying Uncertainty in Activity Volcano Relationships for Oxygen Reduction Reaction. *ACS Catal.* **2016**, *6*, 5251–5259.

(81) Lim, H.-K.; Shin, H.; Goddard, W. A., III; Hwang, Y. J.; Min, B. K.; Kim, H. Embedding covalency into metal catalysts for efficient electrochemical corrosion of CO₂. *J. Am. Chem. Soc.* **2014**, *136*, 11355–11361.

(82) Quek, X.-Y.; Filot, I. A.W.; Pestman, R.; van Santen, R. A.; Petkov, V.; Hensen, E. J. M. Correlating Fischer–Tropsch Activity to Ru Nanoparticle Surface Structure as Probed by High-Energy X-ray Diffraction. *Chem. Commun.* **2014**, *50*, 6005–6008.

(83) Shastri, S. D.; Almer, J.; Ribbing, C.; Cederström, B. High-energy X-ray optics with silicon saw-tooth refractive lenses. *J. Synchrotron Radiat.* **2007**, *14*, 204–211.